RESEARCH ARTICLE | OCTOBER 06 2025

Toward video-rate quantum ghost imaging

Special Collection: Single-photon detectors: new physical principles, circuits and applications

Carsten Pitsch ✉ ; Alessia Suprano ; Benjamin Guery ; Francesco Poggiali ; Chiara Michelini ; Henri Haka ; Davide Moschella; Dominik Walter ; Ugo Zanforlin ; Massimiliano Proietti ; Massimiliano Dispenza; Alberto Tosi ; Federica Villa

APL Photonics 10, 100801 (2025)
https://doi.org/10.1063/5.0284755

Toward video-rate quantum ghost imaging

Cite as: APL Photon. 10, 100801 (2025); doi: 10.1063/5.0284755
Submitted: 10 June 2025 • Accepted: 17 September 2025 •
Published Online: 6 October 2025

Carsten Pitsch,[1,a)] Alessia Suprano,[2] Benjamin Guery,[1,3] Francesco Poggiali,[4] Chiara Michelini,[2,5] Henri Haka,[6] Davide Moschella,[6] Dominik Walter,[1] Ugo Zanforlin,[2] Massimiliano Proietti,[2] Massimiliano Dispenza,[2] Alberto Tosi,[6] and Federica Villa[6]

AFFILIATIONS

[1] Fraunhofer IOSB, Gutleuthaussstr. 1, 76275 Ettlingen, Germany
[2] Leonardo Labs, Quantum Technologies Lab, Via Tiburtina, km 12, 400, Rome 00131, Italy
[3] Université Paris-Saclay, Institut d'Optique Graduate School, 91127 Palaiseau, France
[4] Leonardo Electronics Division, Via Delle Officine Galileo 1, Campi Bisenzio 50013, Italy
[5] Department of Physics, University of Trento, via Sommarive 14, 38123 Trento, Italy
[6] Dipartimento di Elettronica, Informazione e Bioingegneria, Politecnico di Milano, Piazza Leonardo da Vinci 32, 20133 Milano, Italy

Note: This paper is part of the Special Topic on Single-Photon Detectors: New Physical Principles, Circuits and Applications.
[a)] **Author to whom correspondence should be addressed:** carsten.pitsch@iosb.fraunhofer.de

ABSTRACT

Quantum Ghost Imaging (QGI) is a powerful imaging technique that enables probing of an object using illumination levels beyond classical limits and does not rely on a single-photon-sensitive camera in the spectrum of interest. Current "heralded" QGI setups provide high-resolution images with intensified charge-coupled device (ICCD) cameras, but their acquisition time and applicability are limited by setup complexity and detector dead time. Recently, new setups using single photon detection and time-tagging have been shown to allow more efficient acquisition while also enabling new applications, such as remote 3D imaging using "asynchronous" QGI. Here, we demonstrate novel results of two asynchronous QGI setups, using a dedicated high duty-cycle single photon avalanche diode array to drastically reduce acquisition time to sub-second regime, demonstrating video acquisition at 10 fps. As this scheme allows interoperability with arbitrary single photon timing detectors, it can be adapted to a variety of applications and is not bound by the detection window of silicon-based detectors. We further study the impact of the choice of bucket detector and pump laser, using readily available off-the-shelf detectors and lasers. Summarizing the findings, we discuss the remaining limitations for real-time imaging and give an outlook on upcoming developments and an outline of further applications of both detectors and detection scheme.

I. INTRODUCTION

Quantum imaging (QI) has recently experienced a surge in interest and advances, leading to a multitude of new applications.[1–3] This is accompanied by a series of developments in the field of single photon detection, allowing us to tailor technologies to dedicated setups and applications. A major advantage exploited by most QI schemes is the possibility to spectrally separate the detected photons (signal) and the interacting photons (idler), allowing imaging without a camera dedicated to the interacting photon.[4–8] Recently, nonlinear interferometry, also known as "imaging with undetected photons,"[9] has become a focus of attention due to the maturity of the necessary technology and the ability to sense without directly detecting the interacting photon.[7,8,10,11] However, the scheme is limited since it involves superposition of two spontaneous parametric downconversion (SPDC) processes and requires indistinguishability between the generated pairs, as well as the need for a controlled measurement environment.[5,12] This leads to challenges related to dispersion and loss, particularly in applications such as remote sensing, and usually limits the setup to applications in transmission configuration, such as microscopy. On the contrary, Quantum Ghost Imaging (QGI) does not rely on interferometric methods but is based on the temporal detection of both photons of one entangled pair. Therefore, it requires two dedicated single-photon detectors,

one for each photon, posing a significant technical challenge. Despite this constraint, the QGI scheme remains robust even under high-loss conditions[13–17] and enables applications in remote sensing and generally in 3D imaging scenarios,[18–20] where such losses are unavoidable. Another fundamental limitation of the current QGI schemes is the acquisition rate. While the so-called "heralding" schemes[21] allow high-resolution imaging, their gated cameras require an image-preserving optical delay line and their usually high dead time leads to long acquisition times.[22,23] Recently, new schemes employing time-tagged single-photon cameras have demonstrated highly efficient imaging across a wide range of applications.[24–27] While some of these schemes have demonstrated acquisition times in the sub-minute regime, those usually relied on the same detector to acquire both photons.[25,26,28] As a result, they are significantly limited in their ability to perform spectrally separated acquisition, a key advantage of quantum imaging. On the other hand, for imaging with two separate detectors, such as asynchronous QGI,[20] the acquisition time has usually been limited to tens of minutes, similarly to that of "heralded" QGI. This is mostly due to the low duty-cycle, i.e., the ratio between the detectors active measurement time per frame and the frame duration (between 1%and 5%), and the limited fill-factor ~5%–20% of the single photon avalanche diode (SPAD) cameras originally developed and designed for Time-of-Flight (ToF) Light Detection and Ranging (LiDAR) applications, such as flood-illumination-based flash LiDAR systems.[29]

Here, we demonstrate results with a high performance SPAD camera, developed specifically for QGI and capable of achieving image reconstruction with acquisition times of ~0.1–1 s, presenting the first images in an asynchronous configuration reconstructed with a frame-rate of ~10 fps, moving toward video-rate imaging. This improvement was achieved by implementing a multi-gate acquisition in a single frame approach, leading to an increase in duty cycle. In addition, the detector was equipped with microlenses to increase the fill-factor. The independent photon detection achieved with such a timing SPAD array makes our approach suitable even for remote sensing. Along with this new camera, we investigate the impact of the accompanying hardware on QGI performance by comparing two distinct setups featuring different equipment, i.e., Fraunhofer IOSB (IOSB) and Leonardo QT Labs (LDO) setups. This includes the bucket detector design and implementation, pump laser parameters, and auxiliary hardware, such as time-tagger performance and computing resources. We further conduct experimental investigations focused on the evaluation of the current setup's efficiency and QGI image resolution capabilities. Moreover, using an efficiency-optimized IOSB setup a first quantum ghost video has been submitted alongside this publication. As an outlook, we discuss the findings of this analysis, potential challenges in real-time imaging, and the necessary developments to address these challenges.

II. SPAD CAMERA

The SPAD camera used for the acquisitions presented in this paper is based on a 32 × 32 SPAD array,[30] fabricated in a 0.35 μm high-voltage CMOS technology (Fig. 1). Although it is a quite old technology node, it offers high-performance SPADs and is a suitable choice for applications where the pixel pitch requirements are more relaxed. The SPAD size in this array is 30 μm in diameter, and

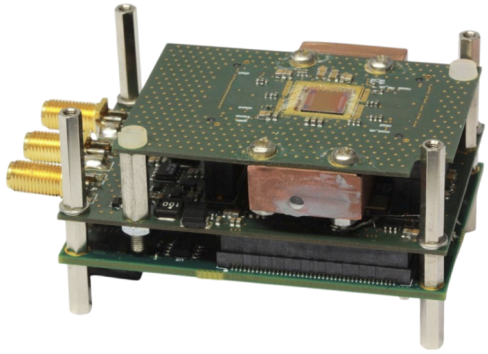

FIG. 1. SPAD camera system.

the pixel pitch is 150 μm, resulting in a 3.14% fill-factor. However, a microlens array mounted on top of the chip recovers the effective fill-factor to 78% with collimated beams. The SPAD peak Photon Detection Probability (PDP) is about 50% at 450 nm and reduces to 40% at 550 nm, corresponding to 30% total Photon Detection Efficiency (PDE), accounting also the losses due to the fill-factor. The Dark Counting Rate (DCR) is extremely low, being about 50 cps at room temperature.[31] The camera offers both Single Photon Counting (SPC) and Time-Correlated Single Photon Counting (TCSPC) readout modalities and can achieve up to 160 kfps. To carry out TCSPC measurements, the array integrates 32 × 32 Time-to-Digital Converters (TDCs), one in each pixel, capable of detecting at most one photon per frame. These TDCs offer a 12 bit conversion with adjustable resolution. The architecture of the TDC consists of two stages, a coarse counter to achieve a long Full Scale Range (FSR) and a 16-phase clock interpolator for a fine resolution, which can be adjusted by tuning the reference clock. The best time resolution that can be achieved is 260 ps with a jitter of 410 ps Full-Width at Half-Maximum (FWHM) and 1 μs FSR. A higher temporal resolution might be useful to reduce the power dissipation of the camera and obtain a higher FSR, at the cost of timing precision.

The TDC implements the sliding-scale technique to improve the conversion linearity, achieving 2% Least Significant Bit (LSB) Differential Non-Linearity (DNL) and 10% LSB Integral Non-Linearity (INL).[31] The sliding scale is implemented by using separate interpolators for the START and STOP signals. The START signal is a shared signal for the whole array, while the STOP signal is synchronous with the event detected by each pixel. An additional feature provided by the array is the multi-gate capability. The multi-gate functionality allows for opening multiple detection gates within the same acquisition frame, thus significantly increasing the duty cycle of the measurement. Theoretically, having a minimum frame duration of 6 μs and a 1 μs FSR TDC, it would be possible to open six gates and thus reach a duty cycle of 100%. Empirically, POLIMI proved that the camera can keep a stable operation without overheating with a duty cycle as high as 80%. Similar SPAD array architectures have been reported in the literature, such as by Eshun *et al.*,[27] which demonstrate comparable performance in the context of QGI, where the primary objective is TCSPC exploiting column shared TDCs. While this approach can reduce implementation complexity, it may increase the likelihood of event collisions, which is

detrimental for the Signal-to-Noise Ratio (SNR) of the QGI measurement. In contrast, the present detector integrates a dedicated TDC in each pixel, thereby minimizing collision-related losses and maintaining the high duty cycle of ~80%. The data stream incoming from the chip is sampled and processed in a Field Programmable Gate Array (FPGA) and stored temporarily in a DDR3 memory chip. The interface between the end user and the camera sensor is made possible by a Graphical User Interface (GUI) application developed in C++. The language was chosen to keep up with the high data rate that the camera yields during each acquisition frame, which averages nearly 390 MB/s. To transfer this amount of data from the FPGA module to the computer running the measurement software, the USB 3.0 protocol is used. Furthermore, the data are stored in binary files, which can be used for post-processing and coincidence detections. Some optimizations have been implemented in order to reduce the size of these files, as data generation can be as high as 2 kB per μs, i.e., about 333 MB/s (at maximum frame-rate). An important optimization used in the measurements presented in this work is to preprocess acquired data and store only useful information. Since QGI is a photon-starved application, i.e., most of the pixels in a frame do not detect photons, only the timestamps of detected photons and their pixel position are saved in the output file, significantly reducing file size.

III. SETUPS

Two asynchronous QGI setups have been implemented independently at both Fraunhofer IOSB and Leonardo QT Labs, as shown in Fig. 2. Both setups used a 2 mm long periodically poled potassium titanyl phosphate (ppKTP) crystal, poled to achieve collinear type-0 phase-matching for 405 nm (pump), 550 nm (signal), and 1550 nm (idler). While the LDO used a large bandwidth laser diode as a pump source ($\Lambda \sim 1.5$ nm), the IOSB used both a laser diode (OBIS, $\Lambda \sim 0.6$ nm) and a single longitudinal mode (SLM, $\Lambda < 0.02$ nm) laser. The pump power was modulated from ~30 μW up to 20 mW during experiments to investigate its impact

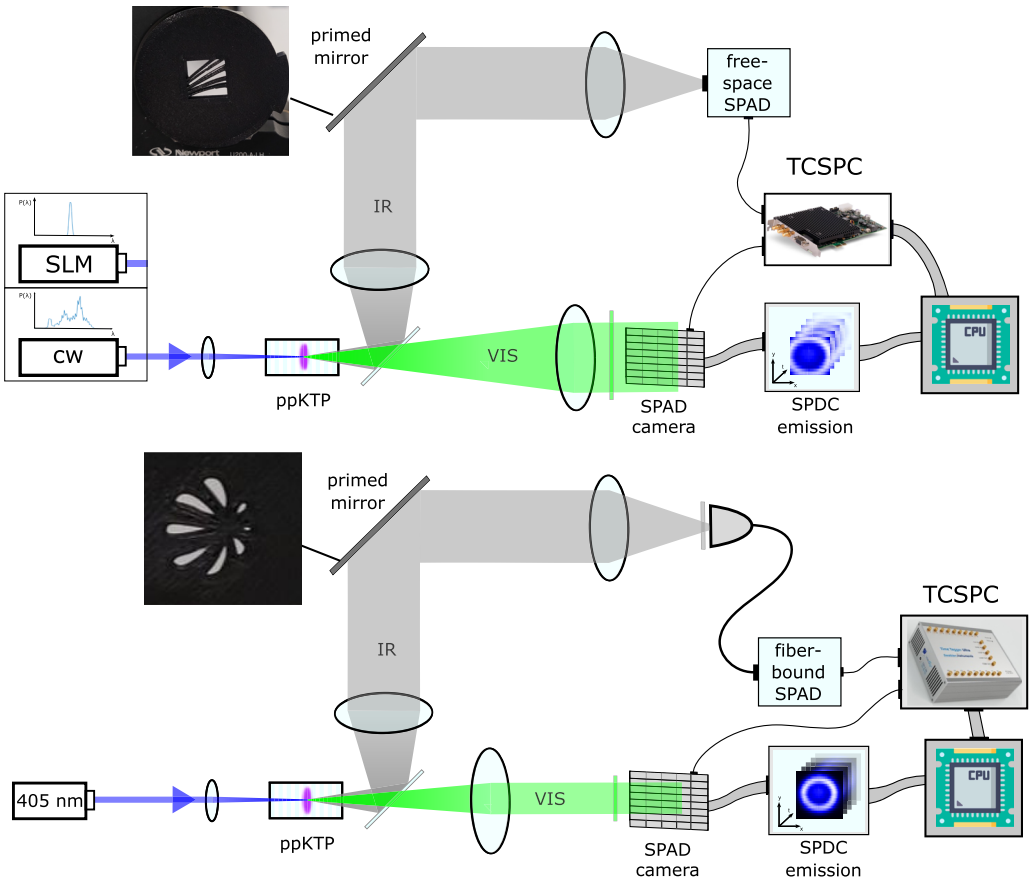

FIG. 2. Optical setups used in this work. Top: IOSB setup. IOSB used two pump lasers, a laser diode and an SLM laser (only one laser was operated at a time, with measurements taken separately for each. Metrological information is given in the supplementary material). The camera was overfilled with the signal emission to use a maximum detector area for coincidence imaging. The idler radiation was detected with a free-space coupled NFAD detector. Bottom: LDO setup. LDO used a 405 nm laser diode with 1.5 nm bandwidth and typically 1.3 mW power. For the sake of clarity, the collimation optical system on the visible branch is shown as a single lens; for further details, see the supplementary material. For the resolution tests, a USAF resolution test target was used (Thorlabs R3L3S1N, see Sec. IV B). The camera was underfilled to maximize photon collection, while the idler radiation was detected using a fiber-bound InGaAs-SPAD detector.

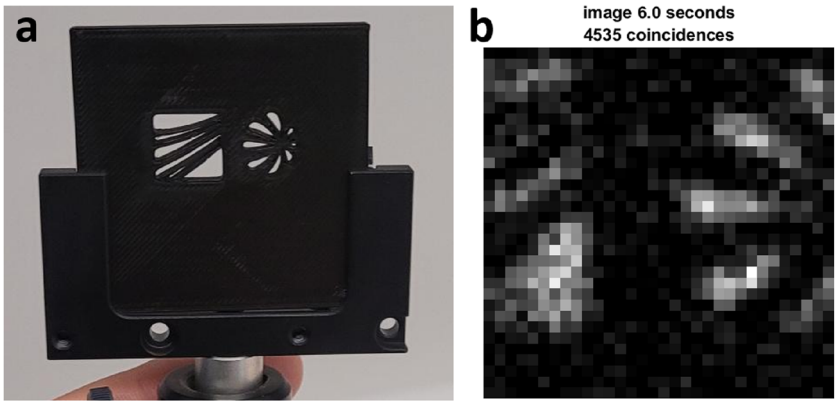

FIG. 3. Demonstration of video-rate acquisition. (a) Transmission mask with FhG and LDO logos, which was moved through the idler beam. (b) Still image of the video, showing parts of both logos. The full video can be found online.

on acquisition time, image quality, and coincidence identification. With a photon conversion efficiency of ~4×10^{-8} for a ppKTP crystal, this corresponds to illumination powers in the idler of ~0.3 to 200 pW.

Both setups used the same SPAD camera (see Sec. II), while the detector for the idler (bucket detector) differed, with the LDO using a relatively large, multimode fiber-bound InGaAs-SPAD with a fiber core diameter of 62.5 μm and the IOSB using a smaller free-space coupled InGaAs negative feedback avalanche diode (NFAD) module with a detector diameter of ~16 μm. The two setups were equipped with different auxiliary hardware and especially with different processing hardware. Thus, the LDO was able to perform measurements with 50% duty cycle at a TDC resolution of 260.8 ps (10 gates with 20 μs frametime), while the IOSB used a duty cycle of 40% at 284 ps resolution (12 gates with 30 μs frametime). More details on the setups can be found in the supplementary material, along with a demonstration of near-video-rate acquisition at ~10 fps (see also Fig. 3).

IV. RESULTS

The key difference between the IOSB and LDO setups lies in the selection of the bucket detector. Since collection efficiency is primarily influenced by the numerical aperture of the collection optics and the detector size, the free-space design simplifies the coupling of the idler emission, while the larger core size in the fiber-based design enhances collection efficiency. Notably, the IOSB free-space detector has a numerical aperture 3.63 times that of the LDO fiber-based detector, whereas the fiber-based detector size is 3.9 times larger than its free-space counterpart. As a result, comparable collection performances are expected from both designs.

As a comparative experiment, both setups performed imaging with their respective diode laser set to 10 mW. Both groups imaged their respective institution's logos using transmission masks, with the IOSB logo having a transmission of t_{mask} ~ 50%, while the LDO logo has t_{mask} ~ 35%. The excess bias voltage of the bucket detector was set to pre-calibrated values (calibrated by the manufacturer) corresponding to the PDP of η_{IR} = 25% for IOSB and η_{IR} = 20% for LDO. The reconstructed images are shown in Fig. 4 (top and bottom). Since the LDO and IOSB setups employed slightly different parameters for the detectors and the transmission mask, we will compensate for these losses to ensure a fair comparison. Accounting for losses due to mask transmission (t_{mask}) and detector efficiency (η_{IR}), it is possible to define the bucket detector heralding efficiency as

$$\frac{CR}{S_{VIS}} \frac{1}{t_{mask}\eta_{IR}}, \tag{1}$$

where CR is the coincidence rate and S_{VIS} is the single count rate of the SPAD array. Likewise, the camera heralding efficiency can be defined as

$$\frac{CR}{S_{IR}} \frac{1}{\tau\eta_{pixel}}, \tag{2}$$

where CR is the coincidence rate, S_{IR} is the single count rate of the IR detector, τ the duty cycle, and η_{pixel} is the PDE of the SPAD pixels. Both LDO and IOSB OBIS setups achieve a bucket heralding efficiency of ~1% with a camera heralding efficiency of 18%. Since LDO and IOSB OBIS setups are characterized by similar features for both photon sources and optical setups, the same value for the bucket heralding efficiency suggests a comparable collection efficiency of the bucket detector, which should be the primary limitation of its heralding efficiency.

Despite this low efficiency, image acquisition is still possible with a coincidence rate of 760 Hz/mW$_{\text{pump}}$ for the IOSB logo and 1.44 kHz/mW$_{\text{pump}}$ for the LDO logo. These coincidence counts are sufficient for image reconstruction with a frame-rate of 1 fps (IOSB) to 10 fps (LDO), as shown in Fig. 4 (first and third rows).

By substituting the OBIS laser with an SLM laser, the acquisition of the IOSB setup could be improved by roughly an order of magnitude, yielding a coincidence rate of ~7.1 kHz/mW$_{\text{pump}}$ (camera heralding efficiency of 31% and bucket detector heralding efficiency of ~4%). This also improved the frame-rate possible with the IOSB setup by an order of magnitude to ~10 fps. The results obtained with a pump power of 9 mW and a bucket detector efficiency of 25% are reported in the second row of Fig. 4. These results constitute an improvement in acquisition by roughly two orders of magnitude compared to previous measurements.[19] Furthermore, the camera heralding efficiency is an improvement over previous results[21,32,33] based on the "standard" heralded QGI (~1%–9%, assuming up to ~30% PDE[21,32]). We should note, however, that these cameras are limited to about hundreds of coincidence detections per second.

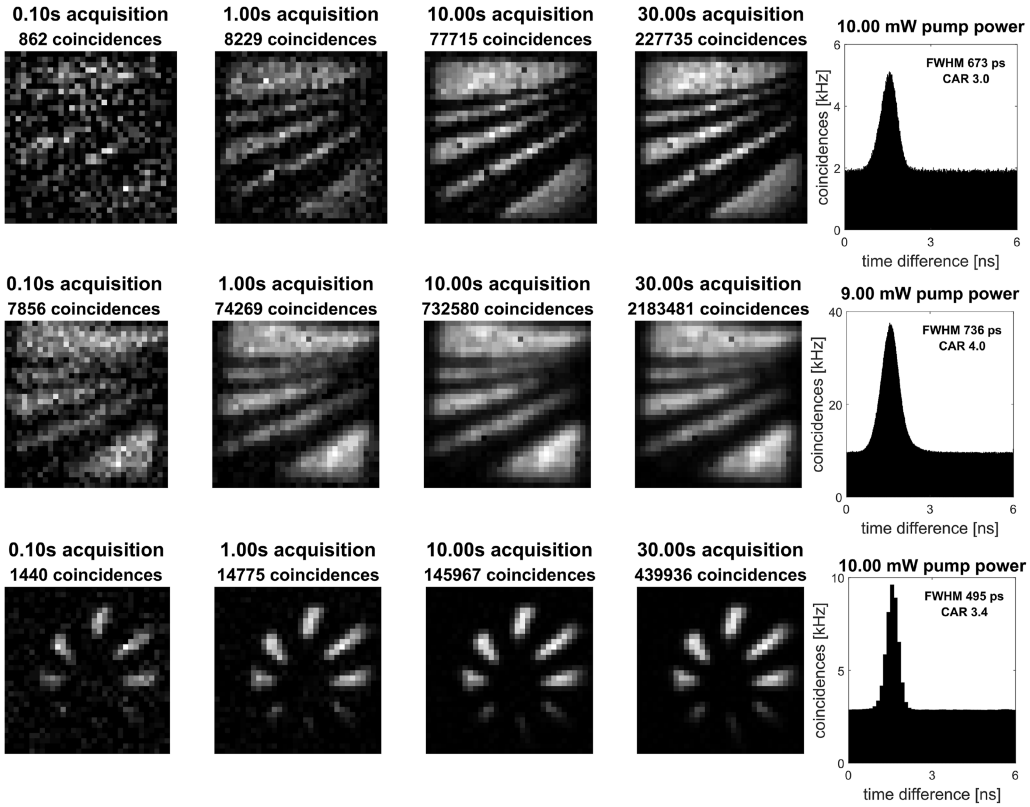

FIG. 4. Comparison between image formation for different setup modalities and acquisition times. Top: Imaging on the Fraunhofer logo with the IOSB setup and an OBIS laser at 10 mW. A coincidence rate of ~8×10^3 Hz was achieved, allowing imaging at a rate of 1 fps. Middle: Imaging with the IOSB setup and an SLM laser at 9 mW. A coincidence rate of ~7.2×10^4 Hz was achieved, allowing imaging at a rate of 10 fps. Bottom: Imaging with the LDO setup on a LDO logo with 10 mW pump power. The coincidence rate of ~1.5×10^4 Hz also enables an image reconstruction rate at ~10 fps.

The gap in bucket heralding efficiency between SLM and OBIS lasers is mainly due to the difference in the collection efficiency of the bucket detector. The SLM laser features a smaller waist and narrower bandwidth, which help to increase the coincidence rate and reduce momentum and frequency dispersion, leading to a smaller idler focus and improving coupling efficiency. Since similar differences have not been experienced in earlier work using fiber-bound detectors,[20] the higher numerical aperture of the free-space detector seems beneficial in this case, despite its lower size. In particular, the spectral width of the OBIS laser will lead to uncertainty in the position of the pump focus, which limits the collimation of the signal and idler emission. This lowers the collection efficiency of small bucket detectors because the spot size of the idler collection optics is significantly enlarged. For long-range imaging, this can also limit image resolution using refractive optics due to non-ideal idler beam collimation. Furthermore, the high bandwidth of the laser imposes additional limitations, reducing performance in spectroscopic applications, such as quantum spectroscopy[34,35] and hyperspectral acquisition.[28]

For the main investigation, IOSB thus used the SLM laser, allowing more efficient collection and acquisition. A more detailed comparison between both laser sources can be found in the supplementary material.

The results obtained with both IOSB and LDO setups are a proof of the reliability, robustness, and video-rate capability of all the methods pursued in this work. A first demonstration of the video-rate capability of this system has been realized with the IOSB setup and the SLM laser at 9 mW pump power and 20% bucket PDP, and can be found online alongside the supplementary material. The video was acquired by moving a transmission mask, shown in Fig. 3, through the idler beam during measurement. It was evaluated at a rate of 10 fps, achieving up to 10.000 coincidences/(video-frame). Further improvements toward a "true" video-rate (20 fps or higher) and real-time image processing are expected with a new camera currently in fabrication (see also Sec. V).

The video-rate capability demonstrates that the proposed setups have significant potential for applications in various scenarios. However, it is crucial to quantify the key performance metrics of the protocol. In Sec. IV A, we will present an analysis of efficiency and temporal resolution conducted by the IOSB SLM setup, which is characterized by highest coincidence rates. Moreover, in Sec. IV B, a characterization of spatial resolution and an analysis of its

limitations and possible enhancements are performed using the LDO setup.

A. Setup efficiency and temporal resolution

As shown in Fig. 5(a), the IOSB SLM setup achieved imaging with coincidence-rates from 10 to 26 kHz/mW$_{pump}$ using pump powers from ~0.1 to 20 mW. The images obtained with 1–7.8 mW pump power (illumination power between 10 and 78 pW) are shown in Fig. 6. It is interesting to note that these illumination powers are roughly on the order of the natural background illumination of a 1-inch target in the same spectral window at night (~50–500 pW; details in the supplementary material[36]). A selection of further measurements conducted to obtain Fig. 5(a) with illumination powers from 0.8 to 172 pW can be found in the supplementary material.

To evaluate the temporal resolution of the system, we analyzed the coincidence peaks achieved by their Full-Width at Half-Maximum (FWHM). This is limited by the temporal jitter of both detectors and can be estimated by the square root of their product.[37] While the jitter of the SPAD camera is fixed, the jitter of the infrared (IR) bucket detector is strongly dependent on its detection efficiency, with higher efficiencies significantly reducing the timing jitter, due to increased reverse bias voltage.[31,38] The FWHM is further limited by the skew of the camera detector, meaning a possible drift of the temporal information of individual pixels. This is a common problem and can depend on many factors. A skew between measurement gates, dependent on the number of gates and frame time, was observed for this detector. This was determined to broaden the base of the coincidence peak by roughly 500 ps to ~2.5 ns and the FWHM by ~100 ps. Through an analysis similar to C. Pitsch *et al.*,[39] performed using a lookup table after some calibration measurements and thus easily implementable even in real-time application, this behavior could be compensated for. This compensation yields a coincidence peak with ~2 ns base width and FWHM between 660 and 800 ps, as shown in Fig. 5(b). For a 3D imaging scheme, the compensation improved the depth resolution by ~1.5 cm, resulting in a final resolution of ~10–12 cm.

Another key aspect of QGI protocols is the signal-to-noise ratio, usually expressed as the Coincidence-to-Accidental Ratio (CAR). It relates the maximum of coincidence counts in the peak to the mean value of the "accidental" coincidences ("noise baseline" in Fig. 6, right panels), giving a measure of "detectability" of the peak itself. It further gives a measure of accidental detections present in the acquired image, whose impact is comparable to that of shot noise. For all measurements, a CAR well above 1 was achieved. Notably, lower detection efficiencies typically resulted in higher CAR values, due to reduced noise from idler photon detections. Especially in the low power regime (<0.5 mW), efficiencies above 25% should be avoided, since the noise counts are orders of magnitude above the actual detections [see Fig. 5(c)]. While the amount of noise in the image can be limiting, the overall detection-rate is of course crucial for short acquisition times. Although not linearly, the coincidence rate continuously increased with pump power until it started saturating at ~10–12 mW. At this power, the camera load was as high as ~50%–60% for each frame. Therefore, since a pixel can only register one photon per measurement frame, we expect that above this threshold, the amount of undetected photon pairs highly increases. To improve this behavior and allow imaging with higher photon throughput, the frame time can be lowered, the amount of gates can be reduced, or the number of pixels can be increased (for more details, see the supplementary material). To allow this, development toward a high duty cycle array with a single gate and four times the pixels is currently under way at POLIMI (see also Sec. V).

The coincidence rate as a function of the bucket detector efficiency does not exhibit a monotonic trend: it rises as expected for low efficiencies, but eventually drops for values higher than 25% [see Fig. 5(a)]. This is due to the highly increased noise of the bucket detector at high excess voltages, which suppress the possible idler detections.

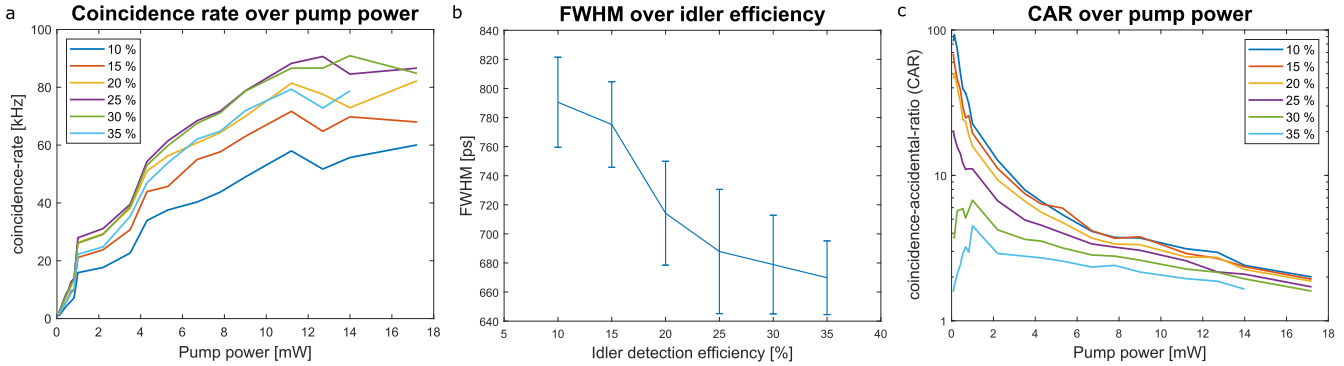

FIG. 5. Overview of system performance using the SLM setup from IOSB. (a) Coincidence rate over pump power. The coincidence rate plateaus at roughly 90.000 Hz and improves with PDP until a value of 25%. For higher values, the detector noise limits coincidence identification and reduces the actual coincidences measured. (b) FWHM of the coincidence peak at different levels of bucket PDP. The FWHM drops by ~120 ps, improving the possible depth resolution by about 15%. Considering the full peak width, the improvement becomes even larger since low PDP operation leads to significant tails.[31] (c) Coincidence-to-accidental-ratio over pump power. The values for detection probabilities below 25% show similar performance, as detector noise does not affect the measurement. For probabilities above 25%, noise can become a significant issue, particularly for low photon pair rate.

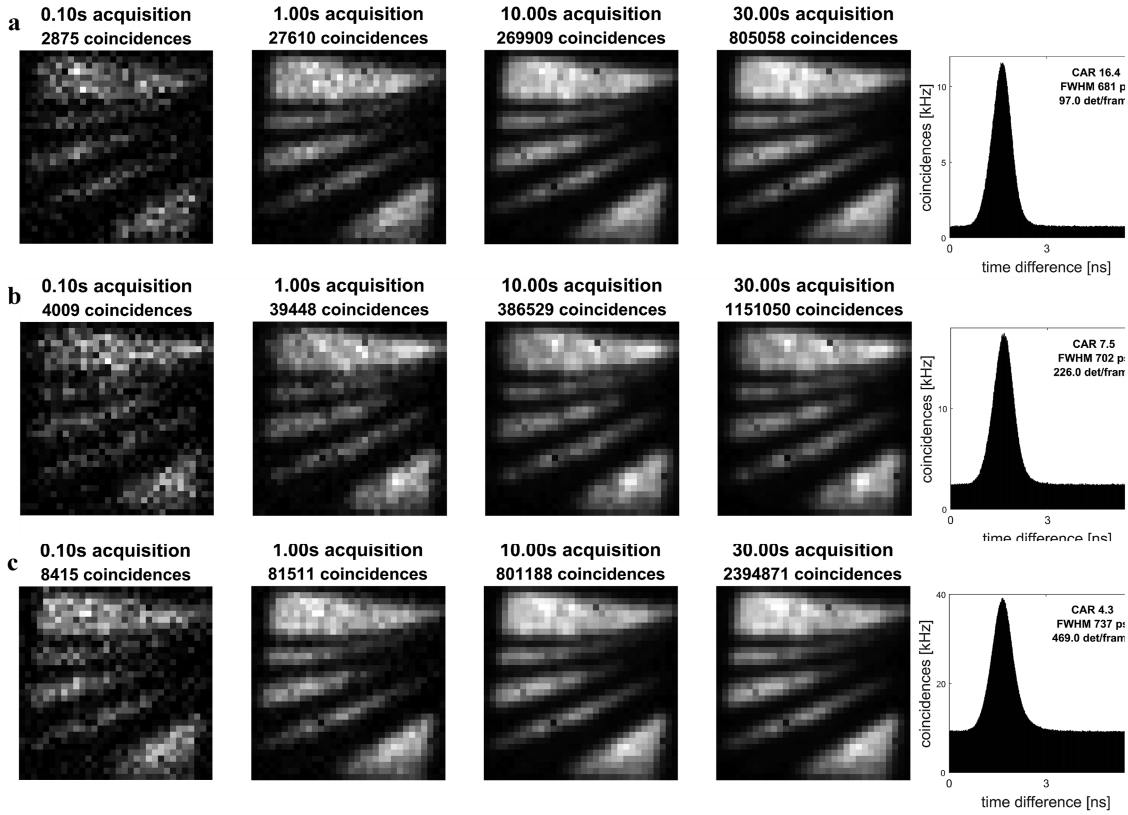

FIG. 6. Comparison of coincidence evaluation and image formation at different pump power levels. The bucket PDP has been set to 20% for all measurements. From top to bottom: (a) 1 mW, (b) 3.5 mW, and (c) 7.8 mW pump power, corresponding to ~10, 35, 78 pW idler illumination power.

Overall, a bucket detection efficiency of 20%–25% represented the best trade-off between low peak FWHM, high CAR, and a maximum number of coincidences over acquisition time. Depending on the application, the weight of these contributions to the QGI performance might change, leading to different optimized sets of parameters.

B. Spatial resolution

Spatial resolution is a key metric to assess the quality of imaging systems. A typical figure of merit used for its evaluation is the visibility v of the image (a.k.a. Michelson contrast),[40] defined as

$$v = \frac{I_{\max} - I_{\min}}{I_{\max} + I_{\min}}, \tag{3}$$

with $I_{\max}$ ($I_{\min}$) being the maximum (minimum) intensity of the area where a target is absent (present). Then, standard periodic targets may be used to test the response of the system as a function of the spatial periodicity. USAF resolution test targets are typical benchmarks in this regard. The LDO used a 3 in. ×3 in. negative USAF target (Thorlabs R3L3S1N) with a group of line pairs (lps) characterized by a periodicity from 0.250 to 228.0 lp/mm. Some reconstructed images obtained by illuminating different USAF regions and changing the acquisition time are reported in Fig. 7(a).

In Fig. 7(b), we studied the visibility of the imaging system as a function of the acquisition time. Notably, line pairs characterized by a periodicity maximum of 0.500 lp/mm can reach a visibility that exceeds the 60% threshold, including its uncertainty, even for the acquisition time of 0.1 s. By increasing the acquisition time, better visibilities are obtained even for higher periodicity. The maximum spatial frequency distinguishable by our setup, and thus the corresponding resolution, is 0.891 lp/mm. Moreover, in Fig. 7(c), the visibility is reported as a function of the line densities by integrating for 24 s and the experimental trend is compared with theoretical simulations.

To accurately simulate the expected behavior, it is essential to consider three key aspects: the characteristics of the source, the optical design, and the intrinsic resolution of the SPAD array camera (for more details, see the supplementary material). The green line in the figure is obtained by considering only the first two aspects, while the simulation mesh is set to 201 × 201 and an infinite statistics is assumed. With these parameters, we simulated the intrinsic resolution of the photon source, which is primarily limited by momentum correlations. In particular, the visibility remains above zero up to ~3 lp/mm and stays consistently above 70% in the range [0.3, 0.9] lp/mm, but this is incompatible with the trend of the experimental results. By binning the simulation outcome into a 32 × 32 matrix, the limitation of the SPAD array camera is taken into account and

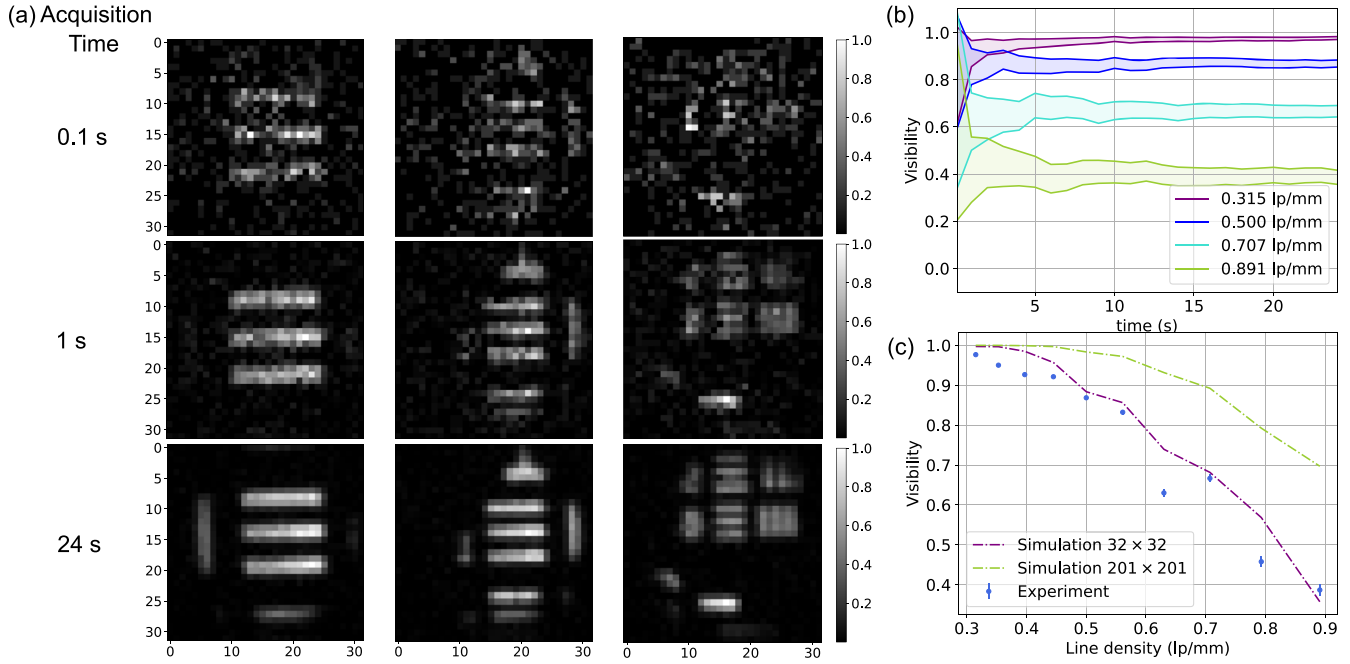

FIG. 7. Study of the spatial resolution of the system as a function of SPAD array camera acquisition time and USAF target line density. (a) Comparison of images obtained for different acquisition times and USAF target regions. The columns from left to right refer to USAF groups with line densities of 0.315, 0.500, and 0.891 lp/mm. (b) Visibility study as a function of camera acquisition time. The colors indicate different target line densities. The shaded regions represent the uncertainty area of the experimental data. (c) Image visibility as a function of the line density of the target. The acquisition time was set to 24 s. The purple (green) dashed line is a simulation of the expected visibility over a 32×32 (201×201) pixels array obtained by assuming the experimental spatial correlation resulting from the experimental optical design and source features (see the supplementary material).

the purple curve is obtained. The result closely reflects the data trend obtained during the experiments (blue scatter). Thus, the main limitation for the visibility analysis in our current experimental setting appears to be the number of SPAD array pixels. Further details can be found in the supplementary material. In this regard, a new SPAD array 64×64 with higher resolution is currently under development. The resolution simulation was obtained following Ref. 41, in which a monochromatic pump beam was assumed (see the supplementary material). Therefore, similar results can be expected for IOSB configurations using OBIS and SLM lasers, even though the latter have a narrower bandwidth.

V. SUMMARY AND OUTLOOK

Video acquisition, especially in real-time operation, relies on three fundamental elements: short acquisition times, high-speed data processing, and fast image reconstruction. In this paper, we demonstrated the usefulness of high duty cycle SPAD cameras for acquisition time in asynchronous quantum ghost imaging. We proved image acquisition at 10 fps, achieving video-rate level in the infrared for the first time. We also characterized the temporal and spatial resolution of QGI systems on two different experimental setups, proving the reliability and robustness of this method.

For our current table-top experiments, coincidence identification and image reconstruction do not represent a major limitation. However, IOSB and LDO are going to implement and test compressive sensing algorithms to boost the reconstruction time also for lower coincidence rate levels. This will be relevant in many practical high-loss scenarios, such as remote sensing. Regarding data processing, while video acquisition is possible with the current QGI scheme, the coincidence evaluation cannot be performed in real-time yet. It instead has to be performed after acquisition, taking ~2–10 times the acquisition time. Although newer versions of TCSPC hardware offer advantages for the system, since issues such as missed timestamps and the need for data corrections are significantly reduced, their capability of real-time processing the data acquired is still in question.

To cover the gap and enable real-time imaging, POLIMI is currently developing a new detector array. This detector will be equipped with a signal input connected to a dedicated TDC for the bucket detector, effectively creating a "virtual pixel" for the idler detections. This allows for the acquisition of the ToF of the idler photons by the SPAD array, obviating the need for a common TCSPC for synchronization. Since the ToF measurements between idler TDC and SPAD array TDCs are already synchronized to the same time frame, i.e., they have the same absolute time reference, they can be processed directly. This is expected to highly simplify data acquisition and processing and to enable real-time coincidence detection and imaging. This detector is expected to be available by the end of 2025, with possible integration of FPGA-based evaluation hardware currently in discussion at IOSB.

The improved iteration of the detector provides more pixels with a 64 × 64 geometry and has an event-driven readout approach, meaning that only pixels that have detected a photon inside an acquisition frame will be read. This leads to the same optimized measurement data as the current SPAD array but does not require extra time or computation for data readout, since data reduction is achieved at hardware architecture level. This drastically decreases the amount of data per frame and relaxes the data bandwidth requirements of the current detector.

Fraunhofer IOSB and LDO are investigating more applications for quantum ghost imaging, with a focus on remote sensing applications. While the IR spectrum shows some advantages due to turbulence resistance,[42] the bucket detectors in this regime are currently limited, being either fiber-bound or relatively small in active area. For remote sensing scenarios using diffuse reflection, this is quite disadvantageous due to the limited collection efficiency. LDO and IOSB are currently working on schemes to enable such scenarios and obtain further metrological information, bringing asynchronous quantum ghost imaging forward. A focus of this work will be the exploitation of the spectral correlation of photons and the realization of the hyperspectral image acquisition.

For further improvements, IOSB plans to investigate the pump laser source and its focus parameters to ascertain its impact on image acquisition. Moreover, LDO is planning to implement a more efficient optical collection of the idler photons. This is in line with the upcoming developments of QGI techniques for the application with reflective or diffusive targets.

SUPPLEMENTARY MATERIAL

More information on the setups and their configuration can be found online in the supplementary material, along with a description of their differences in lasers, hardware, data processing, and detector workload. It also contains additional information on the simulation of resolution performed using LDO and further coincidence measurements performed using IOSB, showcasing performance under various illumination levels.

ACKNOWLEDGMENTS

LDO gratefully thank Dr. A. Guiggiani and Dr. E. Costa for useful and insightful discussion. This project received funding from the European Defence Fund (EDF) under Grant Agreement No. 101103417 EDF-2021-DIS-RDIS-ADEQUADE, funded by the European Union. Views and opinions expressed are, however, those of the author(s) only and do not necessarily reflect those of the European Union or the European Commission. Neither the European Union nor the granting authority can be held responsible for them.

AUTHOR DECLARATIONS

Conflict of Interest

The authors have no conflicts to disclose.

Author Contributions

Carsten Pitsch and Alessia Suprano contributed equally to this work.

Carsten Pitsch: Conceptualization (equal); Data curation (equal); Investigation (equal); Software (equal); Visualization (equal); Writing – original draft (equal); Writing – review & editing (equal). **Alessia Suprano**: Conceptualization (equal); Data curation (equal); Investigation (equal); Software (equal); Visualization (equal); Writing – original draft (equal); Writing – review & editing (equal). **Benjamin Guery**: Data curation (supporting); Investigation (supporting). **Francesco Poggiali**: Data curation (equal); Investigation (supporting); Writing – original draft (supporting); Writing – review & editing (supporting). **Chiara Michelini**: Data curation (supporting); Formal analysis (lead); Writing – review & editing (supporting). **Henri Haka**: Resources (equal); Writing – original draft (supporting); Writing – review & editing (equal). **Davide Moschella**: Resources (supporting); Writing – original draft (supporting); Writing – review & editing (supporting). **Dominik Walter**: Funding acquisition (equal); Investigation (supporting); Methodology (supporting); Project administration (equal); Supervision (equal); Writing – original draft (supporting); Writing – review & editing (equal). **Ugo Zanforlin**: Funding acquisition (equal); Project administration (equal); Writing – review & editing (supporting). **Massimiliano Proietti**: Funding acquisition (equal); Project administration (equal); Supervision (supporting). **Massimiliano Dispenza**: Project administration (supporting); Supervision (supporting). **Alberto Tosi**: Investigation (supporting); Project administration (supporting); Supervision (supporting). **Federica Villa**: Investigation (supporting); Project administration (equal); Supervision (equal); Writing – original draft (supporting); Writing – review & editing (equal).

DATA AVAILABILITY

The processed data that support the findings of this study are available within the article and its supplementary material.

REFERENCES

[1] P.-A. Moreau, E. Toninelli, T. Gregory, and M. J. Padgett, "Imaging with quantum states of light," Nat. Rev. Phys. **1**, 367–380 (2019).
[2] H. Defienne, W. P. Bowen, M. Chekhova, G. B. Lemos, D. Oron, S. Ramelow, N. Treps, and D. Faccio, "Advances in quantum imaging," Nat. Photonics **18**, 1024–1036 (2024).
[3] M. Genovese, "Real applications of quantum imaging," J. Opt. **18**, 073002 (2016).
[4] M. Kutas, B. E. Haase, F. Riexinger, J. Hennig, P. Bickert, T. Pfeiffer, M. Bortz, D. Molter, and G. von Freymann, "Quantum sensing with extreme light," Adv. Quantum Technol. **5**, 2100164 (2022).
[5] C. Lindner, S. Wolf, J. Kiessling, and F. Kühnemann, "Fourier transform infrared spectroscopy with visible light," Opt. Express **28**, 4426 (2020).
[6] M. Gilaberte Basset, F. Setzpfandt, F. Steinlechner, E. Beckert, T. Pertsch, and M. Gräfe, "Perspectives for applications of quantum imaging," Laser Photonics Rev. **13**, 1900097 (2019).
[7] S. Töpfer, M. Gilaberte Basset, J. Fuenzalida, F. Steinlechner, J. P. Torres, and M. Gräfe, "Quantum holography with undetected light," Sci. Adv. **8**, eabl4301 (2022).
[8] V.-L. Dosan, A. S. Perna, M. G. Basset, S. Töpfer, and O. de Vries, "Simultaneous quantum imaging and spectroscopy with undetected photons," in *Quantum 2.0 Conference And Exhibition, QUANTUM* (Optica Publishing Group, 2024), p. QTu4C.6.
[9] G. B. Lemos, V. Borish, G. D. Cole, S. Ramelow, R. Lapkiewicz, and A. Zeilinger, "Quantum imaging with undetected photons," Nature **512**, 409–412 (2014).
[10] M. Kutas, F. Riexinger, J. Klier, D. Molter, and G. von Freymann, "Terahertz quantum imaging," Adv. Quantum Technol. (published online 2025).

[11] M. Placke, C. Lindner, I. Kviatkovsky, H. M. Chrzanowski, F. Kühnemann, and S. Ramelow, "Fourier-transform mid-IR hyperspectral imaging with undetected photons," in *CLEO 2023, CLEO_AT* (Optica Publishing Group, 2023), p. AM2N.4.
[12] M. Gilaberte Basset, A. Hochrainer, S. Töpfer, F. Riexinger, P. Bickert, J. R. León-Torres, F. Steinlechner, and M. Gräfe, "Video-rate imaging with undetected photons," Laser Photonics Rev. **15**, 2000327 (2021).
[13] D. Walter, C. Pitsch, G. Paunescu, and P. Lutzmann, "Quantum ghost imaging for remote sensing," Proc. SPIE **11134**, 111340W (2019).
[14] D. Walter, C. Pitsch, G. Paunescu, and P. Lutzmann, "Detection and jamming resistance of quantum ghost imaging for remote sensing," Proc. SPIE **11160**, 1116002 (2019).
[15] C. Pitsch, D. Walter, H. Bürsing, and M. Eichhorn, "3D quantum ghost imaging," Proc. SPIE **12740**, 1274006 (2023).
[16] Y.-K. Xu, W.-T. Liu, E.-F. Zhang, Q. Li, H.-Y. Dai, and P.-X. Chen, "Is ghost imaging intrinsically more powerful against scattering?," Opt. Express **23**, 32993–33000 (2015).
[17] P. B. Dixon, G. A. Howland, K. W. C. Chan, C. O'Sullivan-Hale, B. Rodenburg, N. D. Hardy, J. H. Shapiro, D. S. Simon, A. V. Sergienko, R. W. Boyd, and J. C. Howell, "Quantum ghost imaging through turbulence," Phys. Rev. A **83**, 051803 (2011).
[18] C. Pitsch, D. Walter, H. Bürsing, and M. Eichhorn, "Remote quantum ghost imaging," Proc. SPIE **12912**, 129120W (2024).
[19] C. Pitsch, D. Walter, L. Gasparini, H. Bürsing, and M. Eichhorn, "3D quantum ghost imaging," Appl. Opt. **62**, 6275 (2023).
[20] C. Pitsch, "Asynchrones quantum ghost imaging," Karlsruher Institut Für Technologie (KIT) Lasers and Optronics: Materials, Technologies and Applications, Ph.D. thesis (2024).
[21] R. S. Aspden, N. R. Gemmell, P. A. Morris, D. S. Tasca, L. Mertens, M. G. Tanner, R. A. Kirkwood, A. Ruggeri, A. Tosi, R. W. Boyd, G. S. Buller, R. H. Hadfield, and M. J. Padgett, "Photon-sparse microscopy: Visible light imaging using infrared illumination," Optica **2**, 1049 (2015).
[22] P. A. Morris, R. S. Aspden, J. E. C. Bell, R. W. Boyd, and M. J. Padgett, "Imaging with a small number of photons," Nat. Commun. **6**, 5913 (2015).
[23] M. J. Padgett and R. W. Boyd, "An introduction to ghost imaging: Quantum and classical," Philos. Trans. R. Soc., A **375**, 20160233 (2017).
[24] D. P. Ryan, K. Meier, K. Seitz, D. Hanson, D. Morales, D. M. Palmer, B. Hanson, P. M. Goodwin, R. Newell, R. M. Holmes, D. Thompson, and J. Werner, "Infrared quantum ghost imaging of living and undisturbed plants," Optica **11**, 1261 (2024).
[25] D. Davenport, A. Eshun, B. Demory, S. Kiannejad, P. Mos, Y. Lin, M. Wayne, S. Jeppson, A. Wilson, T. Bond, M. Rushford, C. Boley, C. Bruschini, E. Charbon, and T. A. Laurence, "Quantum ghost imaging microscopy depth-of-field study," Opt. Express **32**, 36031 (2024).
[26] A. Mavian, Y. Xu, C. Li, and R. W. Boyd, "Fast quantum ghost imaging with a single-photon-sensitive time-stamping camera," Opt. Lett. **50**, 594 (2025).
[27] A. Eshun, D. Davenport, B. Demory, S. Kiannejad, P. Mos, Y. Lin, T. Bond, M. C. Rushford, E. E. Nuccio, T. J. Samo, P. K. Weber, C. Bruschini, E. Charbon, and T. A. Laurence, "3D quantum ghost imaging microscope," Optica **12**, 1109 (2025).
[28] Y. Zhang, D. England, and B. Sussman, "Snapshot hyperspectral imaging with quantum correlated photons," Opt. Express **31**, 2282 (2023).
[29] F. Villa, F. Severini, F. Madonini, and F. Zappa, "SPADs and SiPMs arrays for long-range high-speed light detection and ranging (LiDAR)," Sensors **21**, 3839 (2021).
[30] E. Conca, I. Cusini, F. Severini, R. Lussana, F. Zappa, and F. Villa, "Gated SPAD arrays for single-photon time-resolved imaging and spectroscopy," IEEE Photon. J. **11**(6), 6803910 (2019).
[31] F. Villa, D. Bronzi, Y. Zou, C. Scarcella, G. Boso, S. Tisa, A. Tosi, F. Zappa, D. Durini, S. Weyers, U. Paschen, and W. Brockherde, "CMOS SPADs with up to 500 μm diameter and 55% detection efficiency at 420 nm," J. Mod. Opt. **61**, 102–115 (2014).
[32] D. S. Tasca, R. S. Aspden, P. A. Morris, G. Anderson, R. W. Boyd, and M. J. Padgett, "The influence of non-imaging detector design on heralded ghost-imaging and ghost-diffraction examined using a triggered ICCD camera," Opt. Express **21**, 30460–30473 (2013).
[33] R. S. Aspden, D. S. Tasca, R. W. Boyd, and M. J. Padgett, "EPR-based ghost imaging using a single-photon-sensitive camera," New J. Phys. **15**, 073032 (2013).
[34] C. Lindner, "Nonlinear interferometers based on spontaneous parametric down-conversion for Fourier-transform mid-infrared spectroscopy," Ph.D. thesis, Freiburg University (2022).
[35] A. Chiuri, F. Angelini, S. Santoro, M. Barbieri, and I. Gianani, "Quantum ghost imaging spectrometer," ACS Photonics **10**, 4299 (2023).
[36] R. Gal, S. Keßler, J. Pérez, D. Steiner, and W. Wittenstein, "Trm4.v3 user manual," Technical Report No. 2021/04, Fraunhofer IOSB Ettlingen, Germany, 2021.
[37] M. Wahl, "Time-correlated single photon counting," in Technical note, see https://www.picoquant.com/images/uploads/page/files/7253/technote_tcspc.pdf.
[38] G. Acconcia, F. Ceccarelli, A. Gulinatti, and I. Rech, "Timing measurements with silicon single photon avalanche diodes: Principles and perspectives [invited]," Opt. Express **31**, 33963 (2023).
[39] C. Pitsch, D. Walter, L. Gasparini, H. Bürsing, and M. Eichhorn, "A method to correct the temporal drift of single-photon detectors based on asynchronous quantum ghost imaging," Sensors **24**, 2578 (2024).
[40] A. A. Michelson, *Studies in Optics* (University of Chicago Press, 1927), google-Books-ID: FXazQgAACAAJ.
[41] J. Fuenzalida, A. Hochrainer, G. B. Lemos, E. A. Ortega, R. Lapkiewicz, M. Lahiri, and A. Zeilinger, "Resolution of quantum imaging with undetected photons," Quantum **6**, 646 (2022).
[42] G. Jobert, N. Vannier, S. Pelletier, R. Delubac, X. Brenière, N. Péré-Laperne, and L. Rubaldo, "SWIR's advantage over the visible in long-range imaging scenarios: Comparative field trials in a variety of atmospheric conditions," Proc. SPIE **13046**, 1304609 (2024).